Supplementary Materials for

The structure of the yeast mitochondrial ribosome

Nirupa Desai, Alan Brown, Alexey Amunts and V. Ramakrishnan*

*Corresponding author. Email: ramak@mrc-lmb.cam.ac.uk

This file includes:

Materials and Methods

Isolation of yeast mitochondria

Yeast mitochondria were harvested as previously described (*4*). In brief, *Saccharomyces cerevisiae* were grown aerobically in YPG media (1% yeast extract, 2% peptone, 3% glycerol) until an optical density at 600 nm (OD_{600}) of 2. The cells were then centrifuged at 4,500 × *g* for 9 min, the pellet washed with pre-cooled distilled water and further centrifuged for 15 min at 4,500 × *g.* Following weighing of the pellet it was subsequently resuspended in pre-warmed (30°C) DTT buffer (100 mM Tris-HCl pH 9.3, 10 mM DTT) and left for 30 min at 30°C in a shaking incubator. The cells were pelleted by centrifugation at 3,500 × *g* for 10 min at room temperature and resuspended in Zymolyase buffer (20 mM K_2HPO_4-HCl pH 7.4, 1.2 M sorbitol) to an OD_{600} of 0.6. 1 mg Zymolyase-100T (MP Biomedicals, LLC) was added per gram wet weight measured earlier and the solution was shaken slowly at 30°C for 60 min. This was followed by centrifugation at 4,000 × *g* for 15 min at room temperature. The pellet was further resuspended in Zymolyase buffer and centrifuged for a further 15 min at 4,000 × *g.* The pellet was then resuspended in homogenization buffer (20 mM Hepes-KOH pH 7.45, 0.6 M sorbitol, 1 mM EDTA) and lysed with 15 strokes in a glass homogenizer. To separate the cell debris and nuclei from mitochondria the solution was centrifuged at 2000 × *g* for 20 min and the supernatant collected, followed by further centrifugation at 4500 × *g* for 20 min. Again the supernatant was collected. Centrifugation at 13,000 × *g* for 25 min allowed crude collection of the mitochondrial pellet. Crude mitochondria were further purified on 15-60% step sucrose gradient in SEM buffer (250 mM sucrose, 20 mM Hepes-KOH pH 7.5, 1 mM EDTA) by ultracentrifugation at 141,000 x *g* for 1 hour. Mitochondrial samples were pooled, flash frozen using liquid nitrogen and stored at -80°C.

Purification of yeast mitoribosomes

3 volumes of Lysis buffer (25 mM Hepes-KOH pH 7.5, 100 mM KCl, 25 mM MgOAc, 1.7% Triton X-100, 2 mM DTT) supplemented with 0.0075% Cardiolipin and 100 μg/ml chloramphenicol were added to mitochondria purified from the sucrose gradient and incubated for 10 min on ice. Centrifugation at 30,000 × *g* for 20 min separated out the membrane fraction and the supernatant was loaded on a 1 M sucrose cushion in buffer: 20 mM Hepes- KOH pH 7.5, 100 mM KCl, 20 mM MgOAc, 1% Triton X-100, 2 mM DTT, 0.0075% cardiolipin, 0.05% DDM and 50 μg/ml chloramphenicol. After centrifugation for 4 hours, the pellet was resuspended in the above buffer without Triton X-100 and loaded on a 15%-30% sucrose gradient and run for 16 h at 80,000 × *g*. Mitoribosome fractions were collected and the sucrose removed by passing the sample through a 15 ml concentrator (Vivaspin) with a 30 kDa molecular weight cutoff and

replenishing with the same buffer as above but without Triton X-100 and with 0.001% cardiolipin.

Grid preparation

3 μl aliquots of purified yeast mitoribosomes at a concentration of ~97 nM (0.29 mg/ml) were applied onto 30 s glow-discharged holey carbon grids (Quantifoil R2/2) coated with home-made continuous carbon (~50 Å thick) prior to being blotted for 3.5 s using the FEI Vitrobot. The conditions were set to 100% ambient humidity and 4°C and the grids were flash frozen in liquid ethane prior to transfer into liquid nitrogen for storage.

Electron microscopy

The grids were loaded onto an FEI Titan Krios electron microscope operated at an accelerating voltage of 300 kV. FEI's automated single particle acquisition software (EPU) was used to collect the images, which were recorded on a back-thinned FEI Falcon II detector at a magnification of 104,478 × (resulting in a pixel size of 1.34 Å). 17 movie frames were collected for each 1 s exposure. Defocus values were set from -1 to -3.3 μm. Data were collected in a single session over a 48 h period.

Image processing

The movie frames of each image were aligned using MotionCorr (*31*) prior to estimating contrast transfer function (CTF) parameters using CTFFIND3 (*32*). After manual inspection of the images and their corresponding Fourier transforms a total of 2,525 micrographs were retained. 468,858 particles were selected from these micrographs using semi-automated particle picking in EMAN 2 (*33*). All subsequent image processing was performed using RELION 1.4 (*34*). Reference-free two-dimensional (2D) classification was used to discard 127,588 particles. The remaining 341,270 particles were refined using a 60 Å low-pass filtered map of the unmasked yeast mitoribosome (*4*) as an initial reference. These particles were subsequently corrected for beam-induced particle motion using "particle polishing" in RELION. The nominal resolution after refinement of these 341,270 particles (3.3 Å), and of all other steps, was estimated during post-processing using the Fourier-shell-correlation (FSC) 0.143 criterion (*35*). Binary masks created for post-processing, refinement and classification were generated in RELION with a soft edge applied. High-resolution noise substitution was used to correct for the effects of applying a mask during the FSC calculations (*36*). Before visualization, density maps were corrected for the modulation transfer function of the Falcon II detector and sharpened by applying a negative B-factor that was estimated using automated procedures (*35*).

The polished particles were then refined with a mask applied over the mt-SSU before a first round of 3D classification with the mask maintained. This classification step was performed without further refinement of the assigned angles, which allowed the rapid isolation of classes in which the mt-SSU adopts different orientations. These classes were individually refined before a second round of 3D classification, again without alignment steps. Three well-populated classes were identified (classes A–C, designated on the basis of the number of particles in each class). The best monosome class (class A) resolved to 3.3 Å. The remaining two classes resolved to 3.7 Å and 5.0 Å.

However, even in class A regions of the map were insufficiently resolved to allow for accurate model building. To improve local map density, we generated masks for the mt-LSU, the body of the mt-SSU and the head of the mt-SSU and applied these to separate 3D refinements. The masks of the mt-SSU body and head were applied to 264,961 particles after the first round of classification, while the mask of the mt-LSU was applied to 221,875 particles after the second round of classification. The mt-SSU body had an additional round of 3D classification and 3D refinement. The resulting maps showed improved resolution and local map quality (Fig. S2, B and D).

Additionally, focused classification with signal subtraction (FCwSS) (*37*) was performed on a region of unidentified density above the mRNA exit channel (Fig. S12). Starting with 264,961 particles aligned with a mask over the mt-SSU body, multiple rounds of FCwSS were used to isolate a single class of 153,300 particles in which the density was best resolved.

Model building

The masked maps were used for model building to take advantage of the better local resolution. Gaussian-filtered maps generated using Chimera (*38*) were used to build models in regions of the map with poor density.

Initially, models of the small subunits of the *E. coli* ribosome (Protein Data Bank ID 5IQR) (*39*) and the human mitoribosome (Protein Data Bank ID 3J9M) (*5*) were fitted to the map of the yeast mt-SSU using the "fit in map" function of Chimera (*38*). Each ribosomal protein in the template models was then extracted with those lacking density removed. All subsequent modeling was done in Coot (*40*) . Proteins with homologs in the yeast mitoribosome were rigid-body fitted to the density and modified to the sequence and numbering of the related yeast mitoribosomal protein using sequence alignments from ClustalOmega (*41*). The model was then fitted to the density using real-space refinement. Extensions and insertions were modeled *de novo* in Coot. During model building torsion, planar-peptide, *trans*-peptide and Ramachandran

restraints were applied. Helix restraints were applied during real-space refinement of α-helices. *Trans*-peptide restraints were removed to model *cis*-proline residues for which there were clear density.

Sections of the map without known homologs were interpreted with poly(alanine) models that were then searched against protein databases using PDBeFold (*42*), DALI (*43*) and Backphyre (*44*) to help identify yeast-specific mitoribosomal proteins. Sequences estimated from the density were searched against a list of potential yeast mitoribosomal proteins identified by mass spectrometry or a non-redundant set of protein sequences using protein BLAST (*45*).

Mitoribosomal proteins of the yeast mt-SSU were named according to the recommended nomenclature, as well as mt-LSU protein Mhr1 now renamed to mL67 (*3*). The yeast mitochondria-specific proteins were numbered starting with the lowest number without a prior assignment (mS41) with the proteins ordered by increasing molecular weight.

The 15S rRNA (GenBank ID: KP263414) was built using the model of *E. coli* 16S rRNA (Protein Data Bank ID 5IQR) (*39*) as a template. Using information from an alignment of the two sequences from ClustalOmega (*41*) and their respective secondary structure diagrams (*46*), conserved sections were extracted from the globally fitted 16S rRNA structure and rigid-body fitted to the density to overcome local differences. The sequence and numbering of the bases were then altered to that of *S. cerevisiae* 15S rRNA. Where necessary, these conserved sections were connected by *de novo* modeling. Each nucleotide was inspected and fitted to the density using real-space refinement, often using the "sphere" refinement tool Coot to include all nucleotides in the surrounding environment including the base-paired partner.

To improve the previously published model of the yeast mt-LSU (Protein Data Bank ID 3J6B) (*4*) we first docked the model to the map in Chimera and then optimized the fit using real-space refinement in Coot. Particular emphasis was applied to correcting Ramachandran outliers and regions of the model at the mitoribosome periphery. Previously unbuilt sections of the proteins were modeled where the density permitted. The improved map quality allowed two short regions of the 21S rRNA with registry errors to be identified. Nucleotides 535–557 were renumbered to 531–553 and nucleotides 3005–3039 were renumbered to 3002–3035, with the corresponding sequences changed.

Model refinement and validation

Models for each of the domains (mt-SSU body, mt-SSU head and mt-LSU) were first refined against their respective masked maps to take advantage of the higher resolution information.

The refined models were then combined and further refined against each of the three yeast mitoribosomal classes.

Prior to each refinement, secondary structure restraints for the mitoribosomal proteins were derived from the model using ProSMART (*47*). Basepair, stacking and sugar-pucker restraints were obtained for the rRNA using LIBG (*48*). These external restraints were applied during reciprocal-space refinement in REFMAC v5.8 optimized for cryo-EM maps (*48*). Tighter restraints were applied during refinement against the lower resolution maps to maintain the stereochemistry obtained from the refinements with the higher resolution masked maps. During refinement, the fit of the model to the map density was quantified using $FSC_{average}$ (*48*). Information beyond the nominal map resolution estimated by the FSC=0.143 criterion was excluded during refinement and preserved for validation. The final model-to-map fit was evaluated using $FSC_{average}$ and CRef (*35*). CRef is a measure of the resolution when the FSC between the refined model and map is 0.5.

Post-refinement model statistics were obtained from REFMAC and MolProbity (*49*) and given in table S1. Cross-validation against overfitting was performed as described (*4*, *48*).

Figure preparation

Figures featuring cryo-EM maps were generated using Chimera (*38*). Maps colored by local resolution were generated using estimations of resolution by ResMap (*50*). Figures featuring only models were generated using PyMOL (*51*).

The secondary structure diagram for *S. cerevisiae* 15S rRNA was created by modifying the diagram from the Comparative RNA Website (*46*) with base-pair information extracted from the final model using DSSR (*52*). rRNA helices were labeled according to the equivalent helices in *E. coli* 16S rRNA.

The protein-protein interaction network of the yeast mt-SSU was mapped in two-dimensions using CytoScape (*53*). Molecular weights from UniProt (*54*) were used to represent the nodal size and the edge thickness represents the extent of the protein–protein interface calculated from our model using PDBePISA (*55*).

Table S1. Data and model statistics.

	Class A	Class B	Class C
Data Collection			
Particles	141,795	55,448	24,632
Pixel size (Å)	1.34	1.34	1.34
Defocus mean (μm)	2.4	2.5	2.6
Defocus range (μm)	1.3–4.8	1.3–4.8	1.3–4.8
Voltage (kV)	300	300	300
Electron dose (e·Å^{-2})	23.5	23.5	23.5
Model composition			
Non-hydrogen atoms	201,471	201,471	201,471
Protein residues	13,711	13,711	13,711
RNA bases	4,286	4,286	4,286
Ligands (Zn^{2+}/Mg^{2+})	2/301	2/301	2/301
Refinement			
Resolution (Å)	3.25	3.75	4.97
Map sharpening B-factor (Å^2)	-72.0	-86.6	-138.0
Average B factor (Å^2)	74.9	87.0	111.0
$FSC_{average}$	0.80	0.77	0.72
CRef (Å)	3.37	3.98	5.78
Rms deviations			
Bond lengths (Å)	0.005	0.005	0.005
Bond angles (°)	1.03	1.02	1.02
Validation (proteins)			
MolProbity score	2.0 (100th percentile)	2.1 (100th percentile)	2.0 (100th percentile)
Clashscore, all atoms	2.4 (100th percentile)	3.1 (100th percentile)	2.7 (100th percentile)
Favored rotamers (%)	84.8	84.9	84.7
Poor rotamers (%)	6.0	6.0	6.0
Ramachandran plot			
Favored (%)	94.3	94.4	94.3
Outliers (%)	0.4	0.4	0.4
Validation (RNA)			
Correct sugar puckers (%)	95.3	95.3	95.3
Good backbone conformations (%)	74.5	74.7	74.6

Table S2. Mitoribosomal proteins (MRPs) of the yeast mt-SSU. A similar table for the MRPs of the yeast mt-LSU can be found in (*4*). The MRPs are colored by conservation with the bacterial ribosome (blue) and the human mitoribosome (red) or exclusivity to the yeast mitoribosome (yellow).

MRP	Alias	UniProt ID	Chain ID	Mature protein residue range	MW (Da)	Modeled residues	Notes
bS1m	Mrp51	Q02950	AA	1-344	39,445	2-109, 195-233, 244-299,	Extensively remodeled compared to its bacterial and human mitochondrial counterpart.
uS2m	Mrp4	P32902	BB	26-394	44,162	128-393	
uS3m	Var1	P02381	CC	1-398	47,123	30-68, 78-158, 166-280, 295-398	Encoded by the yeast mitochondrial genome.
uS4m	Nam9	P27929	DD	35-486	56,356	2-80, 88-192, 384-486	
uS5m	Mrps5	P33759	EE	14-307	34,883	14-113, 119-306	
bS6m	Mrp17	P28778	FF	1-131	15,021	1-125	
uS7m	Rsm7	P47150	GG	27-247	27,816	87-247	
uS8m	Mrps8	Q03799	HH	1-155	17,471	2-155	
uS9m	Mrps9	P38120	II	11-278	31,925	35-71, 81-134, 144-278	
uS10m	Rsm10	Q03201	JJ	15-203	23,424	16-201	
uS11m	Mrps18	P42847	KK	60-217	24,563	70-99, 106-217	
uS12m	Mrps12	P53732	LL	21-153	16,917	29-152	
uS13m	Sws2	P53937	MM	1-143	16,089	2-121	
uS14m	Mrp2	P10663	NN	1-115	13,538	1-115	
uS15m	Mrps28	P21771	OO	34-286	33,057	34-112, 128-286	
bS16m	Mrps16	Q02608	PP	1-121	13,639	2-106, 110-120	
uS17m	Mrps17	Q03246	QQ	1-237	27,635	2-117,124-135, 140-150, 159-208, 218-232	
bS18m	Rsm18	P40033	RR	1-138	15,835	40-72, 81-138	

uS19m	Rsm19	P53733	SS	1-91	10,275	9-88	
bS21m	Mrp21	P38175	TT	18-177	20,395	86-177	
mS23	Rsm25	P40496	UU	1-264	30,513	1-233	
mS26	Pet123	P17558	VV	1-318	35,998	2-234	
mS29	Rsm23	Q01163	WW	15-450	50,867	50-450	
mS33	Rsm27	P53305	XX	1-110	12,393	1-96	
mS35	Rsm24	Q03976	YY	31-319	37,393	47-119, 124-319	
mS37	Mrp10	O75012	ZZ	2-95	10,691	5-70, 75-95	Although yeast mS37 shares some similarity to human mS37, it adopts a different spatial orientation. Yeast mS37 contains two pairs of cysteine residues that may form disulfide linkages *in vivo* (*56*), but are not modeled as doing so here due to insufficient density for a disulfide bond.
mS38	Cox24	P32344	11	1-111	12,772	78-111	Not previously identified as a mitoribosomal protein in yeast.
mS41	Fyv4	P38783	22	28-130	15,292	30-128	Sterile alpha motif domain
mS42	Rsm26	P47141	33	1-266	30,224	8-100, 112-262	Forms a heterodimer with mS43. Homologous to Fe/Mn superoxide dismutases.
mS43	Mrp1	P10662	44	14-421	36,729	18-176, 190-230, 244-313	Forms a heterodimer with mS42. Homologous to Fe/Mn superoxide dismutases.
mS44	Mrp13	P12686	55	38-339	38,988	42-78, 115-136	
mS45	Mrps35	P53292	66	27-345	39,575	27-276, 291-345	
mS46	Rsm28	Q03430	77	1-359	41,216	197-361	Occupies a similar position to human mS31 but any structural resemblance appears to be a result of constraints of the environment rather than a shared ancestry.
mS47	Ehd3	P28817	88	36-500	56,288	36-449, 455-492	Probable active enzyme. Structural similar to human 3-hydroxyisobutyryl-CoA hydrolase (HIBCH, PDB entry code 3BPT).

Table S3. Intersubunit-bridge composition. The bridges are colored by conservation with the bacterial ribosome (blue) and the human mitoribosome (red) or exclusivity to the yeast mitoribosome (yellow) and the subset of these found in class B only (teal).

Bridge	mt-SSU	mt-LSU
B1c	uS10m: 43-44, 69 h42: 1379-1380	bL31m: 97-98, 101, 104-105
B2a	h44: 1474-1477, 1586-1599 h45: 1609 h24: 858	H69: 1813-1817, 1819-1820
B2b	h24: 848-850	H68: 1744-1745 21S: 1827-1829
B2c	h24: 835-838 h27: 964-965	H66: 1698-1701 H67: 1738-1741
B3	h44: 1575-1577 1487-1490	H71: 1846-1852, 1859-1861 uL14m: 49-50, 65
B5	h44: 1496-1497	H62: 1656-1657
B6	h44: 1556-1557	bL19m: 155
B7a	h23: 768	H68: 1754-1755
B7b	h23: 778-779 h24: 838-839	uL2m:312, 314-315 274
B8a	h14: 343-345	uL14m: 13, 48, 110, 112-114
mB2	bS6m: 87-90 57-58	uL2m: 228-229, 232-233 247-248
mB3	mS38: 101-102 105-106 109-110	H70: 1832-1834 H71: 1859-1860 H62: 1643-1644 H67: 1739-1741, 1874-1877,
mB7	mS29: 241	H82-ES4: 2389-2390
mB8	uS13m: 56	mL46: 72, 74
mB9	uS13m: 70	uL5: 253-254
mB10R	uS19m: 67 uS13m: 84	uL5: 218-219
mB10	uS19m: 63-67 uS13m: 84	uL5: 218-219, 241
mB11	uS17m: 105-111 uS15m: 77-84, 145 bS6m: 35-36, 74-83 h22:735-736	uL2m: 61-88
mB12	uS15m: 268, 272, 275, 279, 282-283	H42: 613-614 H62: 1639-1640, 1645-1648
mB13	uS13m: 34, 37-38, 41	H62: 1657-1658
mB14	h14:315	bL19m: 166
mB15	mS44: 72, 75-76	bL19m: 135-138
mB16	h44: 1510-1511	H101-ES: 3172

Table S4. Mass spectrometry analysis. Purified yeast mitoribosomes were analyzed by mass spectrometry (*4*) revealing the presence of a number of translational activators and mitochondrial proteins of various functions (others).

mt-LSU	
uL1m	uL30m
uL2m	bL31m
uL3m	bL32m
uL4m	bL33m
uL5m	bL34m
uL6m	bL36m
bL9m	mL38
uL10m	mL40
uL11m	mL41
bL12m	mL43
uL13m	mL44
uL14m	mL46
uL15m	mL49
uL16m	mL50
uL17m	mL53
bL19m	mL54
bL21m	mL57
uL22m	mL58
uL23m	mL59
uL24m	mL60
bL27m	mL61
bL28m	MHR1
uL29m	

mt-SSU
bS1m
uS2m
uS3m
uS4m
uS5m
bS6m
uS7m
uS8m
uS9m
uS10m
uS11m
uS13m
uS14m
uS15m
bS16m
uS17m
bS18m
bS21m
mS23m
mS26
mS29
mS33
mS35
mS37
mS41
mS42
mS43
mS44
mS45
mS46
mS47

Translational Activators
Aep1
Aep2
Atp25
Cbp1
Cbs2
Mam33
Ssc1

Others	
Ach1	Lpd1
Aco1	Lsc2
Ald4	Lsp1
Atp1	Mdh1
Atp16	Mic10
Atp2	Mir1
Atp3	Mss116
Atp4	Ndi1
Atp5	Om45
Atp6	Pda1
Atp7	Pdb1
Cat2	Pdx1
Cit1	Pet9
Cor1	Phb1
Cox2	Phb2
Cox5	Por1
Fum1	Pth4
Ggc1	Qcr2
Gut2	Qcr7
Hsp60	Rip1
Idh2	Sdh1
Ilv5	Sdh2
Kgd1	Stb1
Kgd2	Suv3
Krt14	Tim9
Lat1	

Supplementary figures

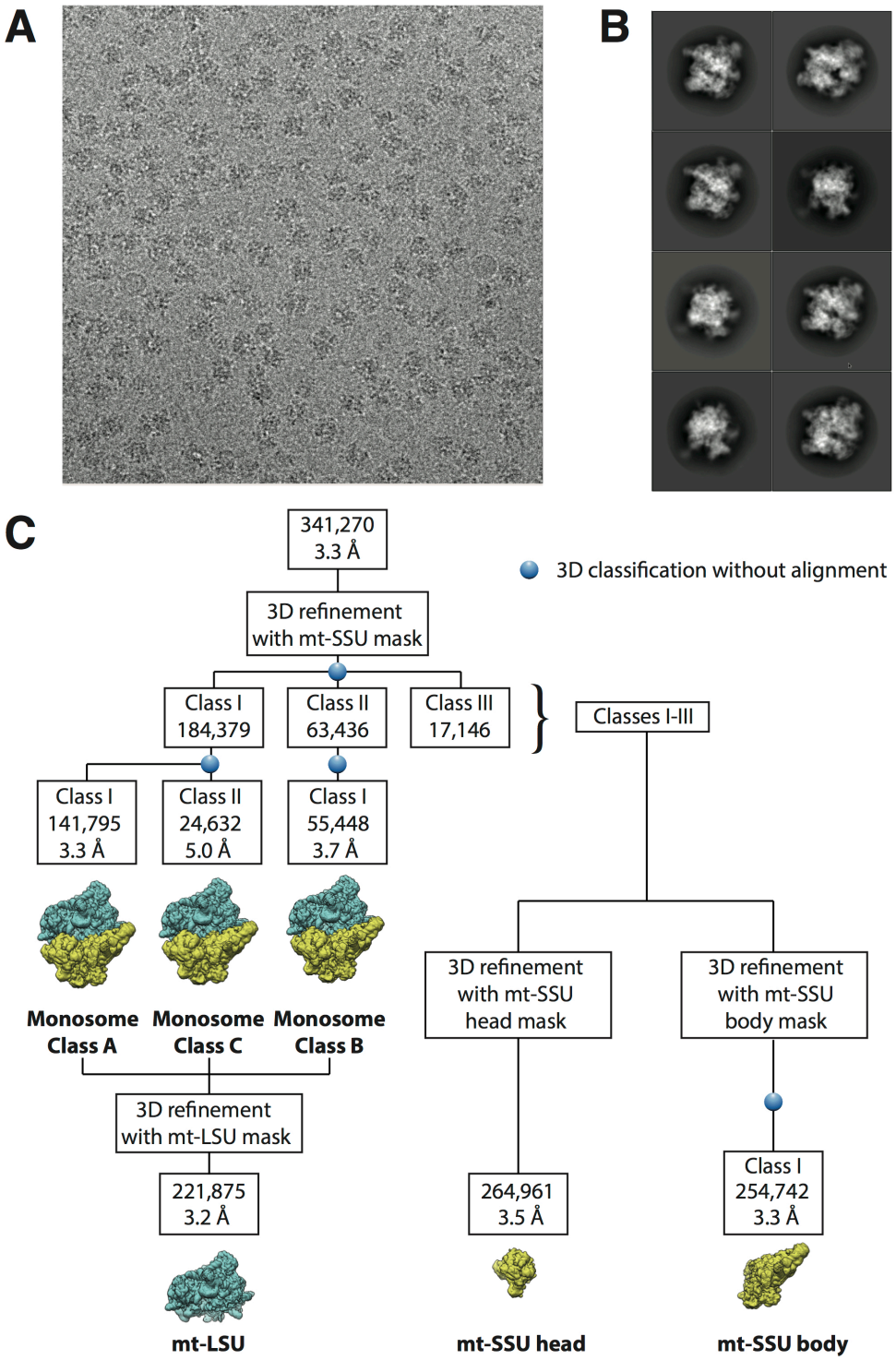

Fig. S1. Electron microscopy data and processing work flow. (A) Representative electron micrograph. (B) Gallery of 2D classes showing different views of the yeast mitoribosome. (C) Data processing steps.

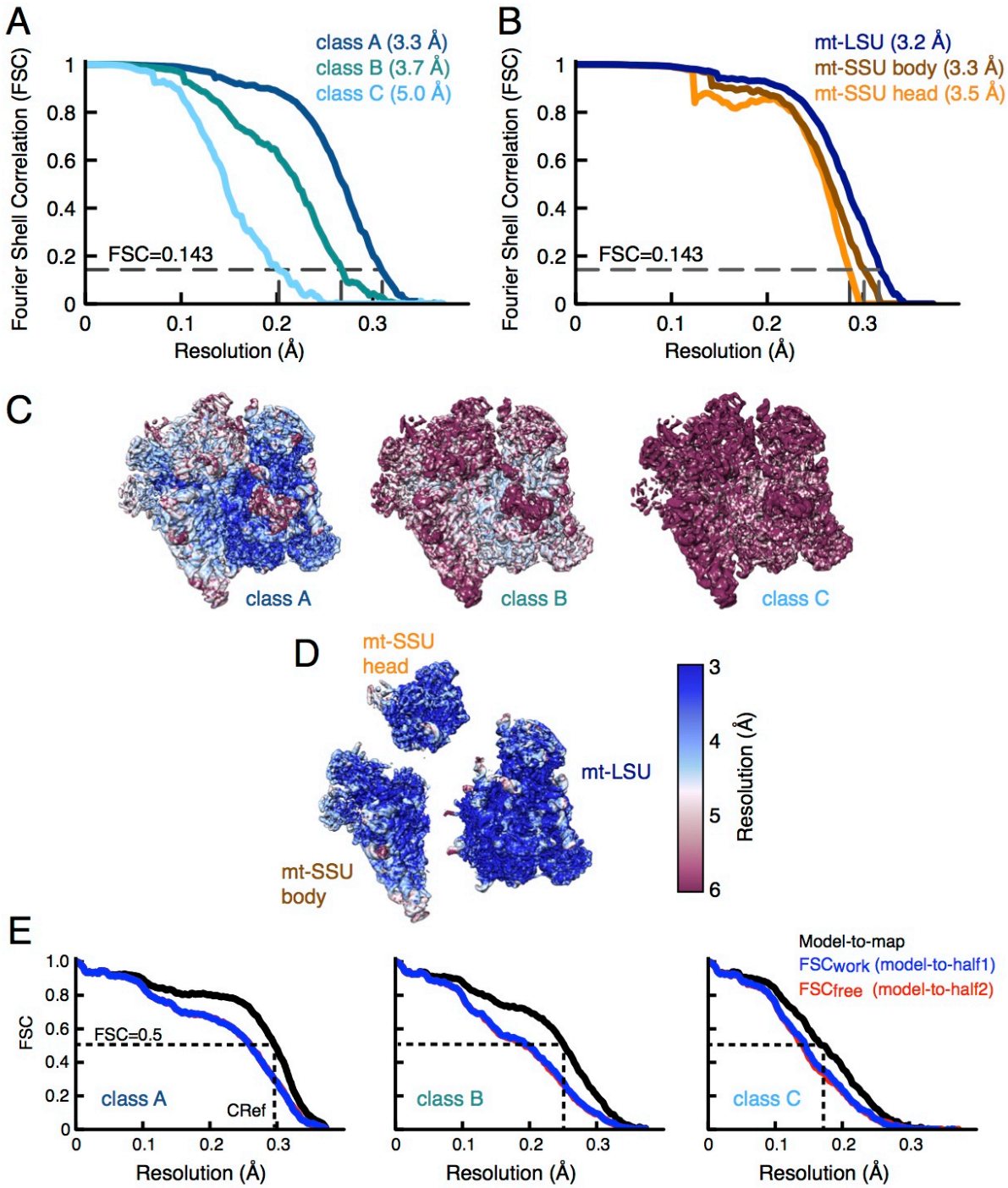

Fig. S2. Map quality. (A) Fourier-shell-correlation (FSC) curves for the three different conformations of the yeast mitoribosome. (B) FSC curves for the masked maps. (C) The map for each class colored by local resolution. (D) The map for each masked map colored by local resolution. (E) FSC curves of the fit of the refined model to the final map (black) for each conformation of the yeast mitoribosome. The resolution at FSC=0.5 (CRef) is indicated with a dashed line. The self- (FSC_{work}) and cross-validated (FSC_{free}) correlations are shown in blue and red, respectively.

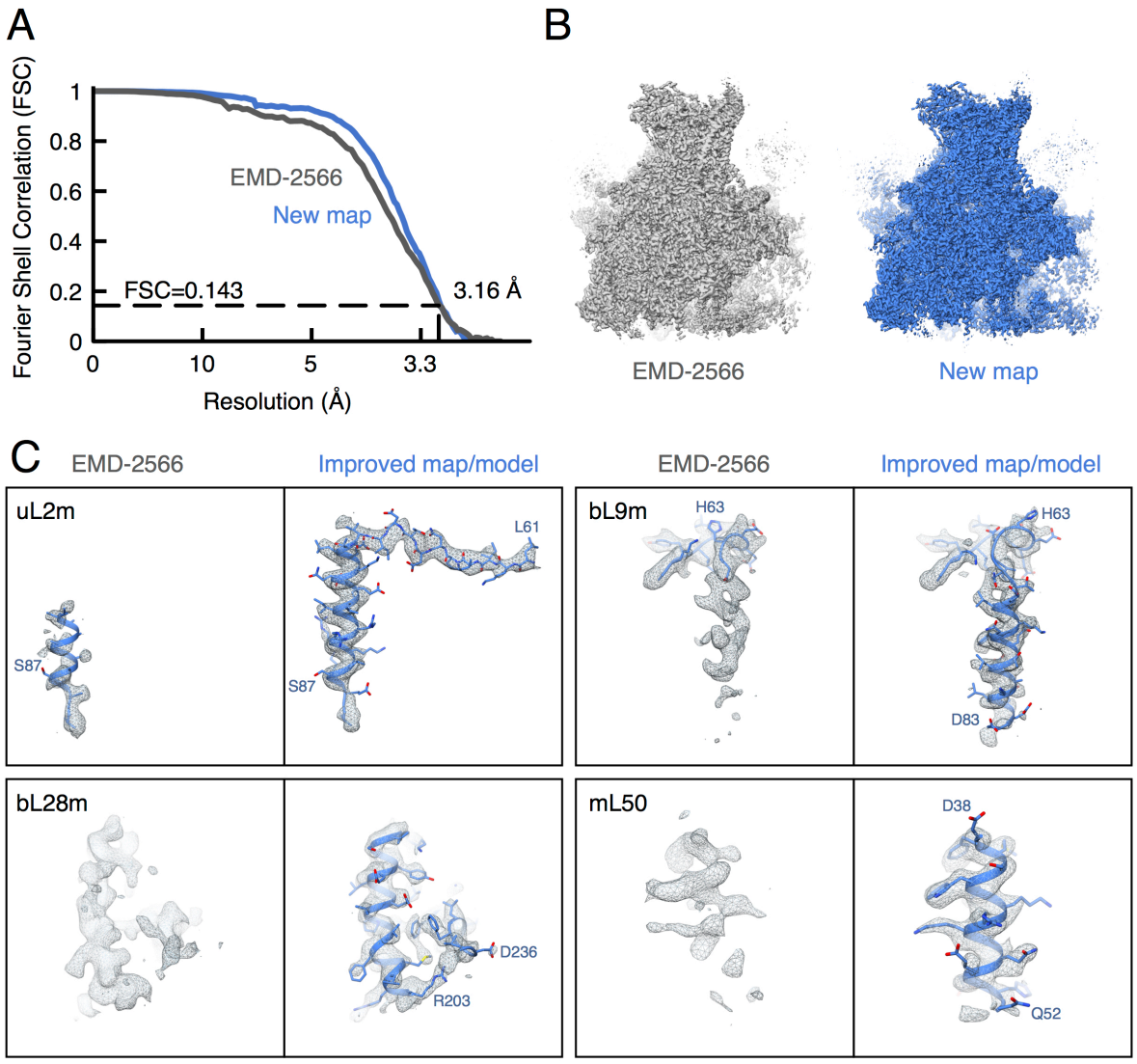

Fig. S3. An improved map for the yeast mt-LSU. (A) Fourier-shell-correlation (FSC) curves comparing the masked map of the yeast mt-LSU with our previously published map (EMD-2566) (*4*). Although the overall resolutions are similar (~3.2 Å, according to the FSC=0.143 criterion) the new map has higher correlations at lower resolutions. (B) Comparison of the final post-processed maps. (C) Examples of regions that could be interpreted with a model as a result of improved map density.

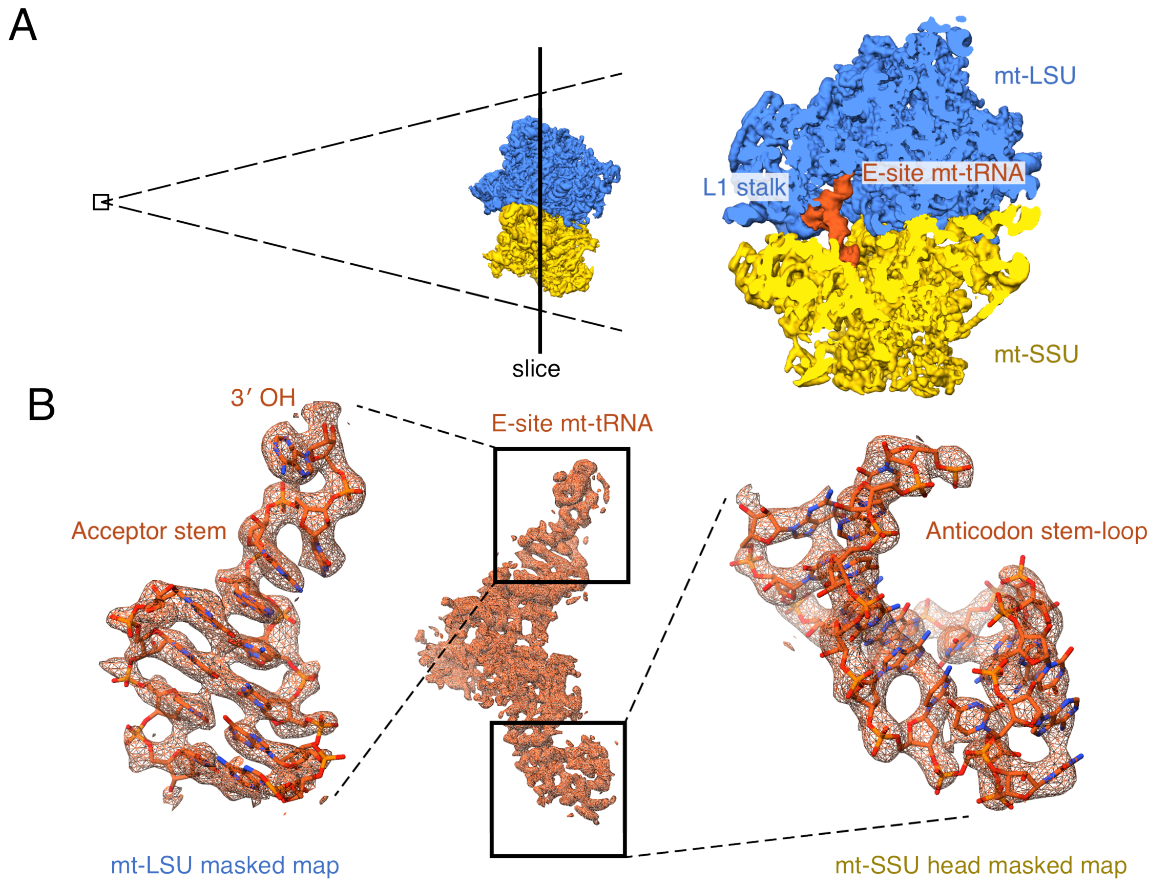

Fig. S4. The yeast mitoribosome co-purifies with an E-site mt-tRNA. (A) Slice through the unfiltered map of the yeast mitoribosome showing an E-site mt-tRNA bound in the intersubunit space that is presumably a mixture of the 24 mt-tRNAs encoded by the yeast mitochondrial genome. The acceptor stem and elbow of the mt-tRNA contacts the mt-LSU, while the anticodon stem-loop contacts the mt-SSU. (B) Sharpened map of the mt-tRNA. Subunit-masked maps were used to model the acceptor and anticodon arms of an unidentified tRNA into the map.

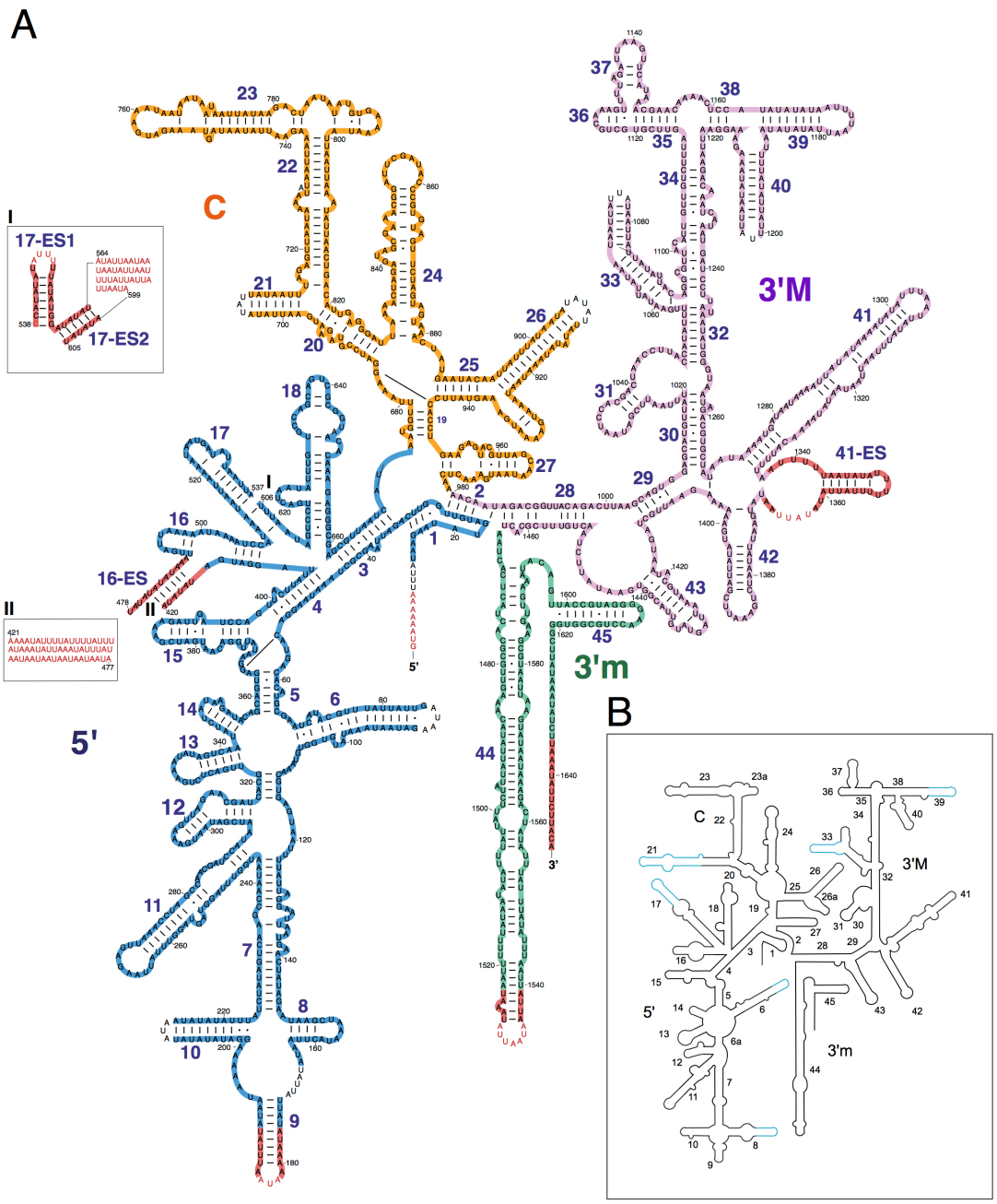

Fig. S5. Secondary structure diagram of the yeast 15S rRNA. (A) 15S rRNA colored by domain. The rRNA expansions specific to the yeast mitoribosome are highlighted in red. Nucleotides that could not be modeled due to poor density are shown with no background coloring. Red lettering is used for unmodeled areas specific to the yeast mitoribosome. (B) Secondary structure diagram of the *E. coli* 16S rRNA with helices not present in the yeast mitoribosome shown in blue.

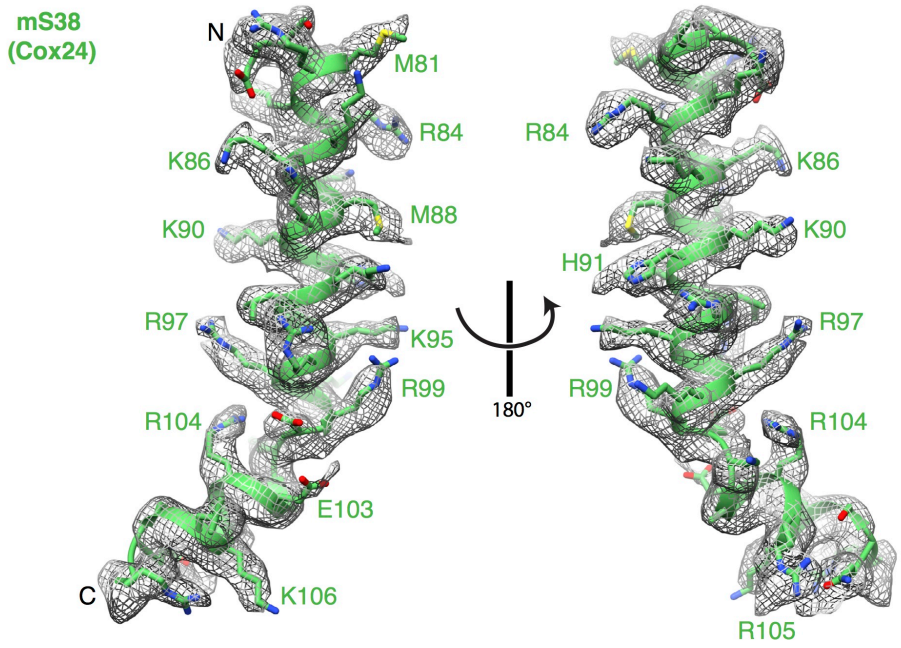

Fig. S6. Fit of the mS38 (Cox24) model to density. mS38 was identified as being a constituent component of the yeast mitoribosome from the density.

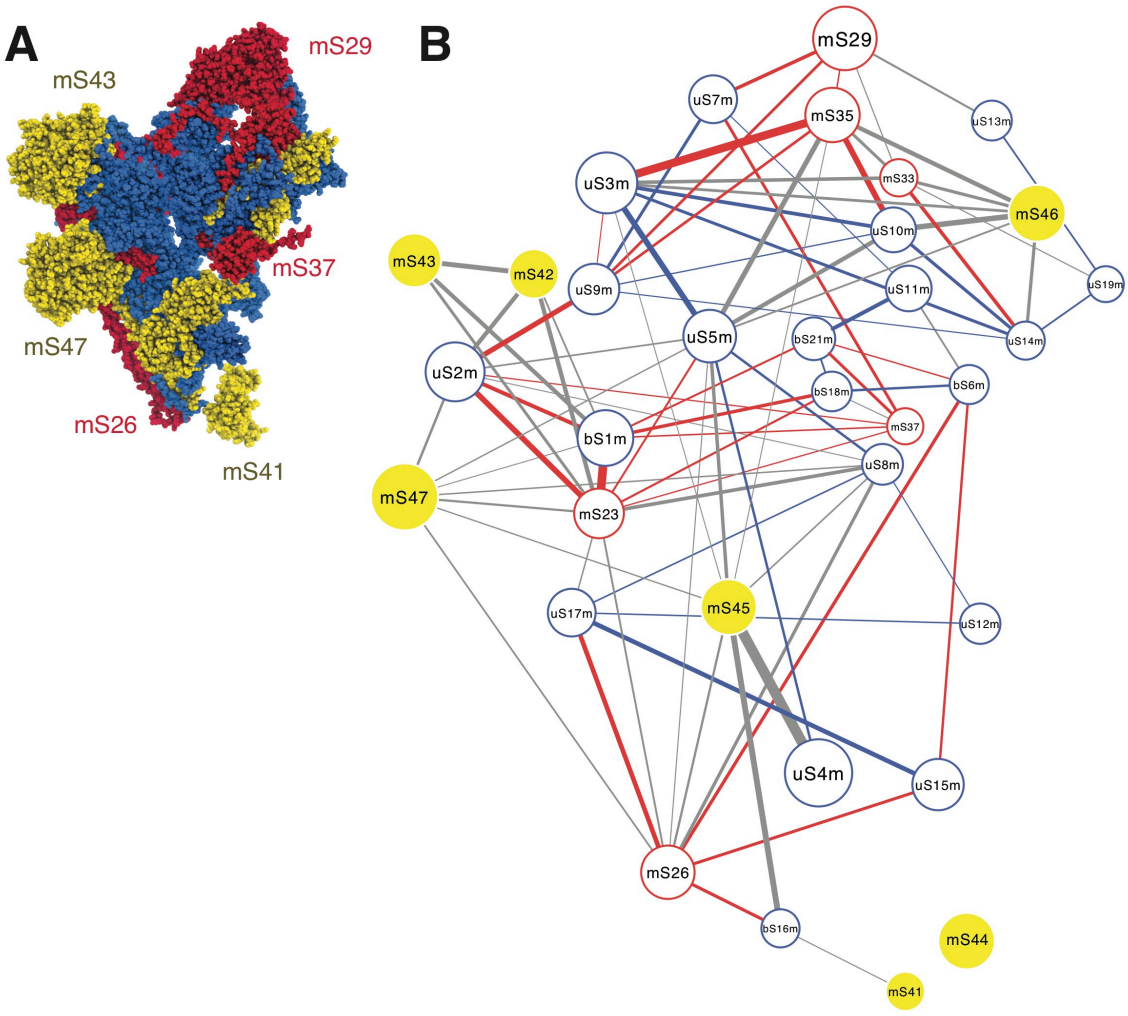

Fig. S7. Interactions between the proteins of the yeast mt-SSU. (A) Yeast mitoribosomal proteins with homologs in the bacterial ribosome are shown in blue and those with homologs in the human mitoribosome are shown in red. Yeast-specific proteins are shown in yellow. (B) The yeast mt-SSU visualized as a protein-protein network. The nodal size represents the relative molecular masses of the mitoribosomal proteins and the edge thickness represents the extent of the interface between interacting proteins. Interactions that also occur in the bacterial ribosome and the human mitoribosome are shown in blue and red respectively. Interactions specific to the yeast mitoribosome are shown in grey. Edgeless nodes represent proteins that contact rRNA only.

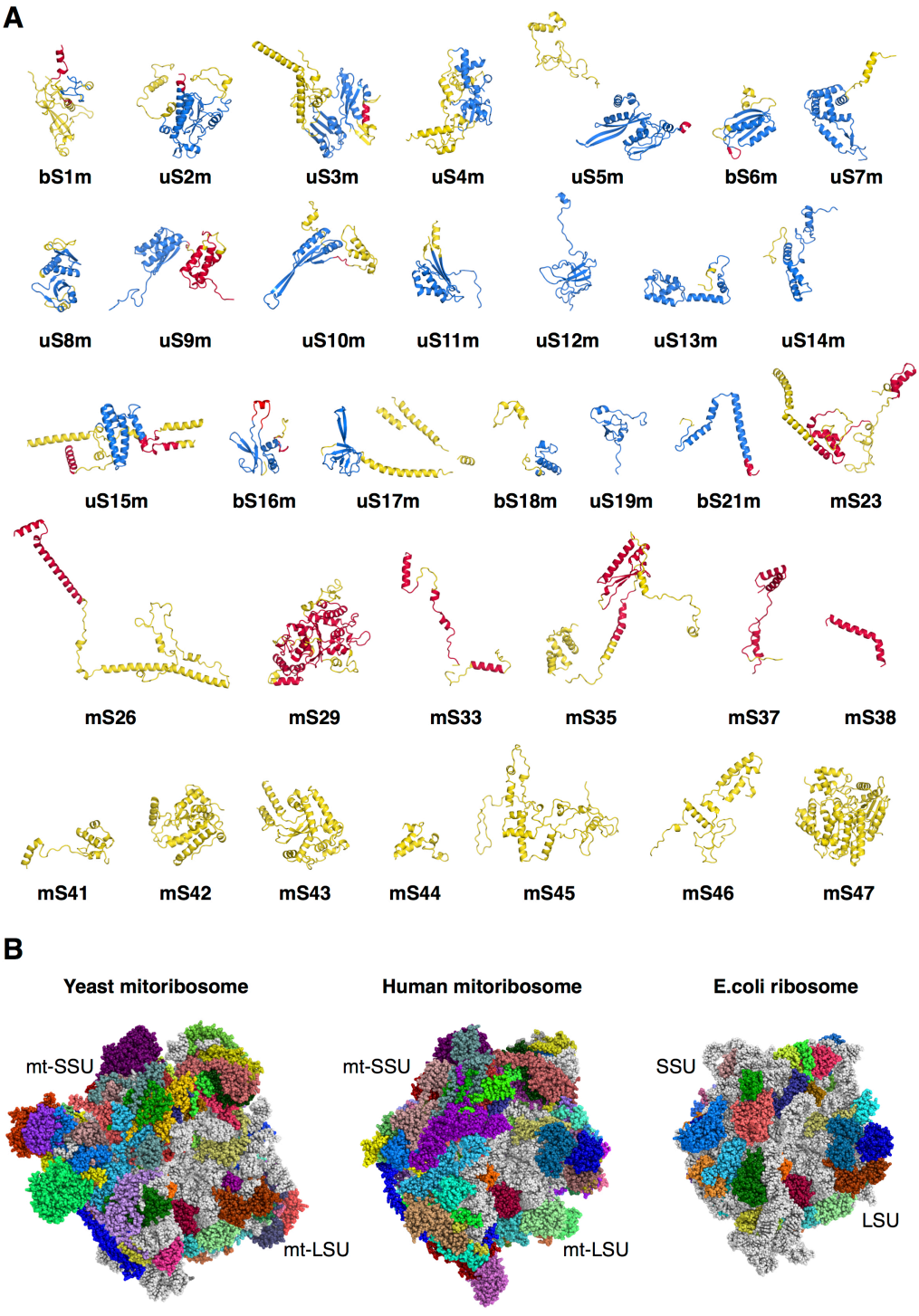

Fig. S8. Mitoribosomal protein expansion. (A) The tertiary folds of each mitoribosomal protein of the yeast mt-SSU colored by conservation. Elements conserved with the bacterial ribosome are colored blue. Elements present in the human mitoribosome but not the bacterial ribosome are colored red. Yeast-specific elements are colored yellow. (B) Distinct protein and rRNA elements give the yeast mitoribosome a distinct architecture compared to the human mitoribosome and the bacterial ribosome.

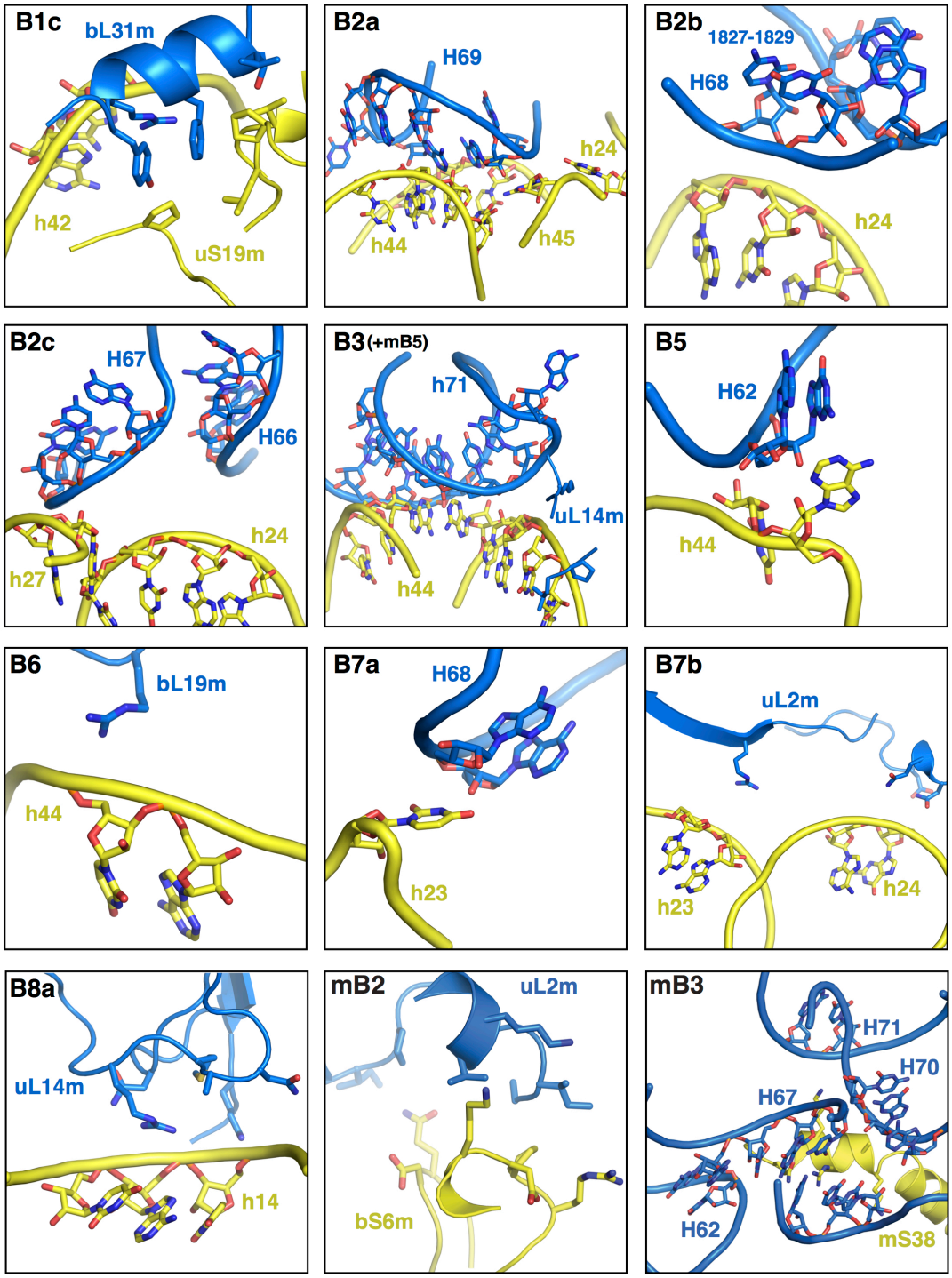

Fig. S9. Bridges conserved with the other ribosomes. Molecular details for each intersubunit bridge of the yeast mt-SSU that either occurs in the bacterial ribosome or in the human mitoribosome. Bridges only present in mitoribosomes are prefixed with an “m”.

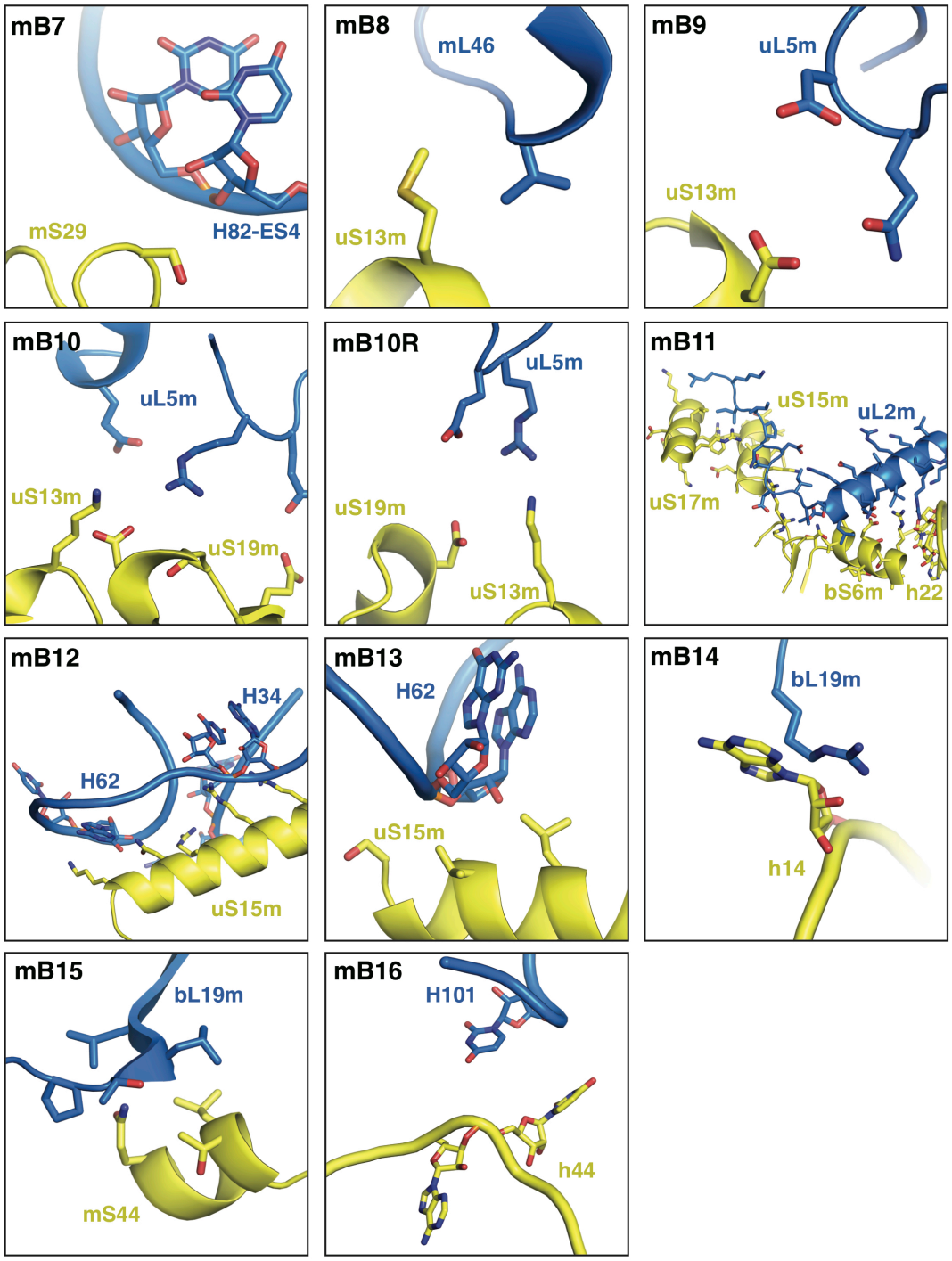

Fig. S10. Bridges specific to the yeast mitoribosome. Molecular details for each intersubunit bridge specific to the yeast mitoribosome. Bridges mB7, mB8, mB9 and mB10R are only present in class B where an 8° rotation of the mt-SSU head results in additional contacts with the mt-LSU.

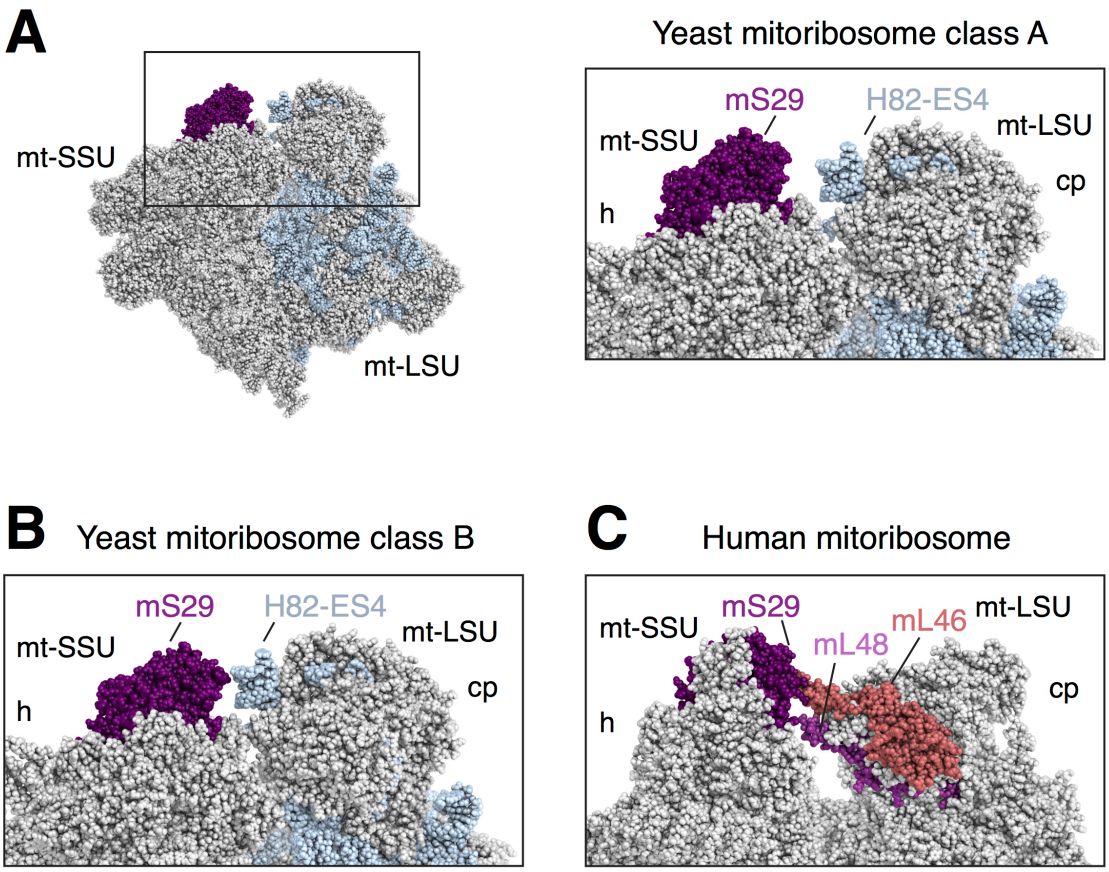

Fig. S11. Comparison of mS29 positions in yeast and human mitoribosomes. (A) Position of mS29 in the yeast mitoribosome class A, with a close up of the boxed section. The boxed sections in panels B and C represent equivalent areas in the yeast mitoribosome class B and the human mitoribosome respectively. (B) Owing to an 8° rotation of the mt-SSU head, mS29 contacts H82-ES4 of the mt-LSU rRNA in the yeast mitoribosome class B (bridge mB7). (C) Equivalent position of mS29 in the human mitoribosome, where the mt-LSU contact is mediated by mL46 and mL48.

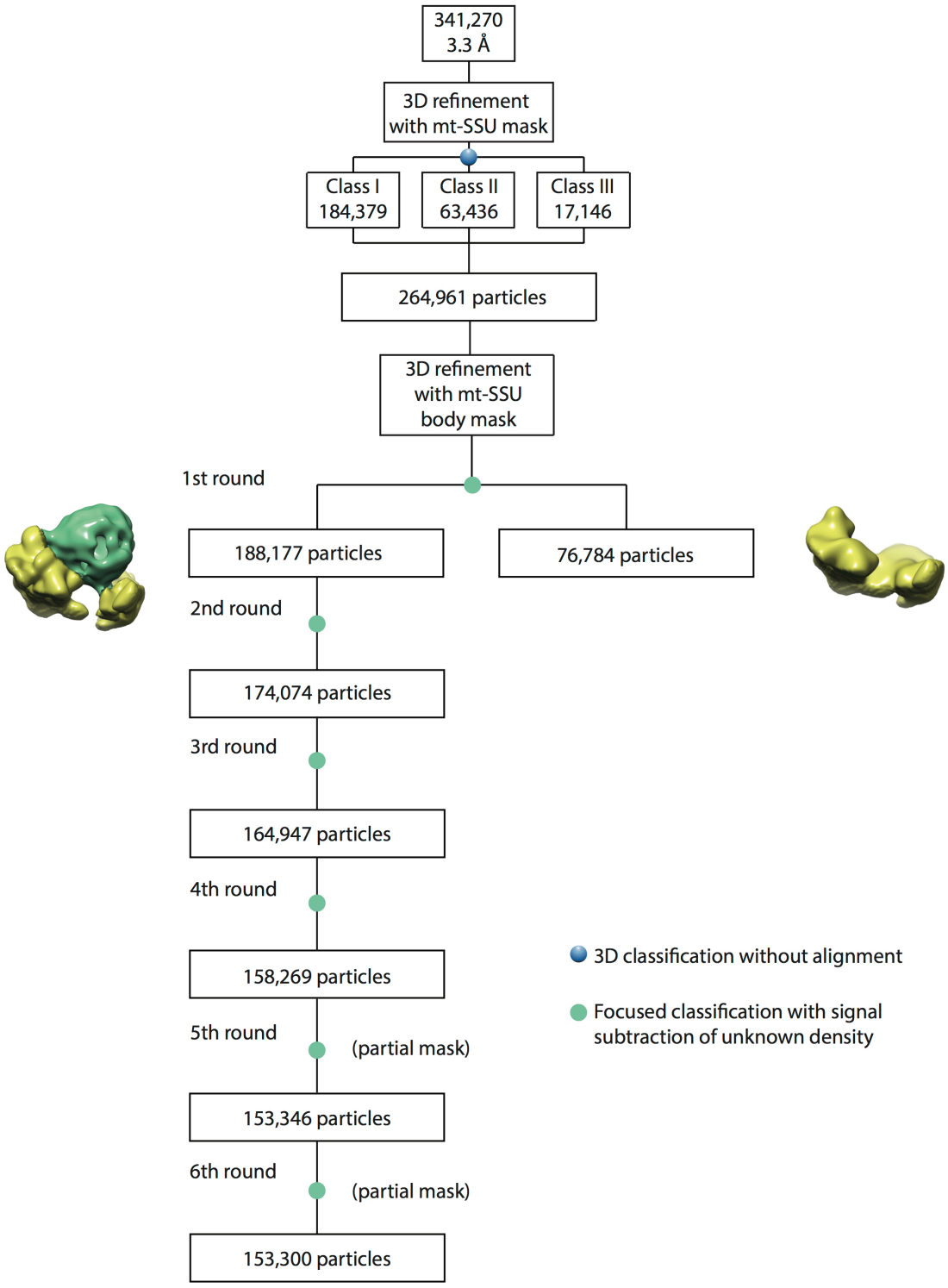

Fig. S12. Classification scheme for the additional density at the mRNA channel exit. Multiple rounds of focused classification with signal subtraction (FCwSS) were used to separate particles containing additional density at the mRNA channel exit from those that did not. Partial mask denotes when only a section of the unknown density was masked.

References

1. M. W. Gray, G. Burger, B. F. Lang, Mitochondrial evolution. *Science*. **283**, 1476–1481 (1999).

2. M. Ott, A. Amunts, A. Brown, Organization and Regulation of Mitochondrial Protein Synthesis. *Annu. Rev. Biochem.* **85**, 77–101 (2016).

3. B. J. Greber, N. Ban, Structure and Function of the Mitochondrial Ribosome. *Annu. Rev. Biochem.* **85**, 103–132 (2016).

4. A. Amunts *et al.*, Structure of the yeast mitochondrial large ribosomal subunit. *Science*. **343**, 1485–1489 (2014).

5. A. Amunts, A. Brown, J. Toots, S. H. W. Scheres, V. Ramakrishnan, Ribosome. The structure of the human mitochondrial ribosome. *Science*. **348**, 95–98 (2015).

6. B. J. Greber *et al.*, Ribosome. The complete structure of the 55S mammalian mitochondrial ribosome. *Science*. **348**, 303–308 (2015).

7. E. O. van der Sluis *et al.*, Parallel Structural Evolution of Mitochondrial Ribosomes and OXPHOS Complexes. *Genome Biol Evol*. **7**, 1235–1251 (2015).

8. J. M. Herrmann, M. W. Woellhaf, N. Bonnefoy, Control of protein synthesis in yeast mitochondria: the concept of translational activators. *Biochim. Biophys. Acta*. **1833**, 286–294 (2013).

9. N. Ban *et al.*, A new system for naming ribosomal proteins. *Current Opinion in Structural Biology*. **24**, 165–169 (2014).

10. J. M. Cherry *et al.*, Saccharomyces Genome Database: the genomics resource of budding yeast. *Nucleic Acids Research*. **40**, D700–5 (2012).

11. G. S. Groot, T. L. Mason, N. Van Harten-Loosbroek, Var1 is associated with the small ribosomal subunit of mitochondrial ribosomes in yeast. *Mol. Gen. Genet.* **174**, 339–342 (1979).

12. C. E. Bullerwell, G. Burger, B. F. Lang, A novel motif for identifying rps3 homologs in fungal mitochondrial genomes. *Trends in Biochemical Sciences*. **25**, 363–365 (2000).

13. M. H. Barros, A. M. Myers, S. Van Driesche, A. Tzagoloff, COX24 codes for a mitochondrial protein required for processing of the COX1 transcript. *J. Biol. Chem.* **281**, 3743–3751 (2006).

14. C. Saveanu *et al.*, Identification of 12 new yeast mitochondrial ribosomal proteins including 6 that have no prokaryotic homologues. *J. Biol. Chem.* **276**, 15861–15867 (2001).

15. M. Kitakawa *et al.*, Identification and characterization of the genes for mitochondrial ribosomal proteins of Saccharomyces cerevisiae. *Eur J Biochem*. **245**, 449–456 (1997).

16. T. C. Petrossian, S. G. Clarke, Multiple Motif Scanning to identify methyltransferases from the yeast proteome. *Mol. Cell Proteomics*. **8**, 1516–1526 (2009).

17. Y. Park, J. S. Bader, How networks change with time. *Bioinformatics*. **28**, i40–8 (2012).

18. G. K. Brown *et al.*, beta-hydroxyisobutyryl coenzyme A deacylase deficiency: a defect in valine metabolism associated with physical malformations. *Pediatrics*. **70**, 532–538 (1982).

19. J. K. Hiltunen *et al.*, The biochemistry of peroxisomal beta-oxidation in the yeast Saccharomyces cerevisiae. *FEMS Microbiol. Rev.* **27**, 35–64 (2003).

20. S. Pfeffer, M. W. Woellhaf, J. M. Herrmann, F. Förster, Organization of the mitochondrial translation machinery studied in situ by cryoelectron tomography. *Nat Commun*. **6**, 6019 (2015).

21. N. D. Denslow, J. C. Anders, T. W. O'Brien, Bovine mitochondrial ribosomes possess a high affinity binding site for guanine nucleotides. *J. Biol. Chem.* **266**, 9586–9590 (1991).

22. G. Z. Yusupova, M. M. Yusupov, J. H. Cate, H. F. Noller, The path of messenger RNA through the ribosome. *Cell*. **106**, 233–241 (2001).

23. M. Selmer, Structure of the 70S ribosome complexed with mRNA and tRNA. *Science*. **313**, 1935–1942 (2006).

24. S. Takyar, R. P. Hickerson, H. F. Noller, mRNA helicase activity of the ribosome. *Cell*. **120**, 49–58 (2005).

25. M. T. Couvillion, I. C. Soto, G. Shipkovenska, L. S. Churchman, Synchronized mitochondrial and cytosolic translation programs. *Nature*. **533**, 499–503 (2016).

26. N. S. Green-Willms, T. D. Fox, M. C. Costanzo, Functional interactions between yeast mitochondrial ribosomes and mRNA 5' untranslated leaders. *Molecular and Cellular Biology*. **18**, 1826–1834 (1998).

27. E. Hajnsdorf, I. V. Boni, Multiple activities of RNA-binding proteins S1 and Hfq. *Biochimie*. **94**, 1544–1553 (2012).

28. P. Haffter, T. D. Fox, Suppression of carboxy-terminal truncations of the yeast mitochondrial mRNA-specific translational activator PET122 by mutations in two new genes, MRP17 and PET127. *Mol. Gen. Genet.* **235**, 64–73 (1992).

29. T. W. McMullin, P. Haffter, T. D. Fox, A novel small-subunit ribosomal protein of yeast mitochondria that interacts functionally with an mRNA-specific translational activator. *Molecular and Cellular Biology*. **10**, 4590–4595 (1990).

30. P. Haffter, T. W. McMullin, T. D. Fox, Functional interactions among two yeast mitochondrial ribosomal proteins and an mRNA-specific translational activator. *Genetics*. **127**, 319–326 (1991).

31. X. Li *et al.*, Electron counting and beam-induced motion correction enable near-atomic-resolution single-particle cryo-EM. *Nat. Methods*. **10**, 584–590 (2013).

32. J. A. Mindell, N. Grigorieff, Accurate determination of local defocus and specimen tilt in electron microscopy. *Journal of Structural Biology*. **142**, 334–347 (2003).

33. G. Tang *et al.*, EMAN2: An extensible image processing suite for electron microscopy. *Journal of Structural Biology*. **157**, 38–46 (2007).

34. S. H. W. Scheres, RELION: Implementation of a Bayesian approach to cryo-EM structure determination. *Journal of Structural Biology*. **180**, 519–530 (2012).

35. P. B. Rosenthal, R. Henderson, Optimal determination of particle orientation, absolute hand, and contrast loss in single-particle electron cryomicroscopy. *Journal of Molecular Biology*. **333**, 721–745 (2003).

36. S. Chen *et al.*, High-resolution noise substitution to measure overfitting and validate resolution in 3D structure determination by single particle electron cryomicroscopy. *Ultramicroscopy*. **135**, 24–35 (2013).

37. X.-C. Bai, E. Rajendra, G. Yang, Y. Shi, S. H. Scheres, Sampling the conformational space of the catalytic subunit of human γ-secretase. *elife*. **4**, 1485 (2015).

38. E. F. Pettersen *et al.*, UCSF Chimera--a visualization system for exploratory research and analysis. *J Comput Chem*. **25**, 1605–1612 (2004).

39. A. Brown, I. S. Fernandez, Y. Gordiyenko, V. Ramakrishnan, Ribosome-dependent activation of stringent control. *Nature*. **534**, 277–280 (2016).

40. P. Emsley, B. Lohkamp, W. G. Scott, K. Cowtan, Features and development of Coot. *Acta Crystallogr. D Biol. Crystallogr.* **66**, 486–501 (2010).

41. F. Sievers *et al.*, Fast, scalable generation of high-quality protein multiple sequence alignments using Clustal Omega. *Molecular systems biology*. **7**, 539 (2011).

42. E. Krissinel, K. Henrick, Secondary-structure matching (SSM), a new tool for fast protein structure alignment in three dimensions. *Acta Crystallogr. D Biol. Crystallogr.* **60**, 2256–2268 (2004).

43. L. Holm, P. Rosenström, Dali server: conservation mapping in 3D. *Nucleic Acids Research*. **38**, W545–W549 (2010).

44. L. A. Kelley, S. Mezulis, C. M. Yates, M. N. Wass, M. J. E. Sternberg, The Phyre2 web portal for protein modeling, prediction and analysis. *Nat Protoc*. **10**, 845–858 (2015).

45. S. F. Altschul *et al.*, Gapped BLAST and PSI-BLAST: a new generation of protein database search programs. *Nucleic Acids Res*. **25**, 3389–3402 (1997).

46. J. J. Cannone *et al.*, The comparative RNA web (CRW) site: an online database of comparative sequence and structure information for ribosomal, intron, and other RNAs. *BMC Bioinformatics*. **3**, 2 (2002).

47. R. A. Nicholls, F. Long, G. N. Murshudov, Low-resolution refinement tools in REFMAC5. *Acta Crystallogr. D Biol. Crystallogr.* **68**, 404–417 (2012).

48. A. Brown *et al.*, Tools for macromolecular model building and refinement into electron cryo-microscopy reconstructions. *Acta Crystallogr. D Biol. Crystallogr.* **71**, 136–153 (2015).

49. V. B. Chen *et al.*, MolProbity: all-atom structure validation for macromolecular crystallography. *Acta Crystallogr. D Biol. Crystallogr.* **66**, 12–21 (2010).

50. A. Kucukelbir, F. J. Sigworth, H. D. Tagare, Quantifying the local resolution of cryo-EM density maps. *Nat. Methods*. **11**, 63–65 (2013).

51. W. L. DeLano, The PyMOL molecular graphics system (2002).

52. X.-J. Lu, H. J. Bussemaker, W. K. Olson, DSSR: an integrated software tool for dissecting the

spatial structure of RNA. *Nucleic Acids Research*. **43**, e142–e142 (2015).

53. P. Shannon *et al.*, Cytoscape: a software environment for integrated models of biomolecular interaction networks. *Genome Res.* **13**, 2498–2504 (2003).

54. UniProt Consortium, UniProt: a hub for protein information. *Nucleic Acids Research*. **43**, D204–12 (2015).

55. E. Krissinel, K. Henrick, Inference of macromolecular assemblies from crystalline state. *Journal of Molecular Biology*. **372**, 774–797 (2007).

56. S. Longen, M. W. Woellhaf, C. Petrungaro, J. Riemer, J. M. Herrmann, The disulfide relay of the intermembrane space oxidizes the ribosomal subunit mrp10 on its transit into the mitochondrial matrix. *Dev. Cell*. **28**, 30–42 (2014).